Materials Science & Engineering A 758 (2019) 47–55

Contents lists available at ScienceDirect

Materials Science & Engineering A

journal homepage: www.elsevier.com/locate/msea

Strengthening of alloy AA6022-T4 by continuous bending under tension

Marko Knezevic[a,*], Camille M. Poulin[a], Xiaodong Zheng[b], Shijian Zheng[b], Irene J. Beyerlein[c]

[a] Department of Mechanical Engineering, University of New Hampshire, Durham, NH, 03824, USA
[b] Shenyang National Laboratory for Materials Science, Institute of Metal Research, Chinese Academy of Sciences, Shenyang, 110016, China
[c] Department of Mechanical Engineering, Materials Department, University of California at Santa Barbara, Santa Barbara, CA, 93106, USA

ARTICLE INFO

Keywords:
Elongation-to-fracture
Strength
Dislocation structures
Continuous-bending-under-tension
AA6022-T4

ABSTRACT

This paper studies the evolution in strength of alloy AA6022-T4 sheets that have been pre-deformed by a continuous-bending-under-tension (CBT) process. Significant improvements in strength are observed only after a few CBT cycles. Less appreciable improvements in strength are observed with more CBT cycles and with every cycle the ductility reduces. These observations are rationalized by characterizing microstructural evolution using transmission electron microscopy and electron backscattered diffraction. It is found that evolution of texture and grain shape during CBT slightly differ from those in simple tension (ST). Also, the precipitates do not change their shape during CBT or ST. It is, therefore, concluded that these microstructural features have only a secondary effect on the strength behavior of the alloy. Consistent with earlier observations in the literature, we find that dislocation structures form within grains during monotonic ST and that they are disorganized and not as well defined. In contrast, cellular substructures are observed to form very early during CBT processing, even after the first cycle and to evolve from loose tangles of dislocations to well-defined walls during subsequent cycles. These dislocation patterns are found responsible for the observed behavior of the alloy. Therefore, the strength of the material is determined not only by the achieved effective strain level but also by achieved microstructure.

1. Introduction

In order to achieve lighter and more crashworthy structural components for vehicles, advanced materials are being developed and incorporated into current designs [1–7]. A primary example of such materials is the aluminum alloy AA6022-T4. Much attention has focused on understanding and optimizing of the microstructure of automotive category Al alloys in order to achieve higher strength, work hardening rate and formability, along with higher energy absorption during crash loading conditions [8–10]. These structural properties are governed by microstructural features, such as precipitates, grain structure, texture, and dislocation structures. To simultaneously improve strength and ductility, these features are being tuned by microstructural design. On the other hand, innovative sheet metal forming processes are being developed to extend the elongation to failure of the material, thwarting localized necking and subsequent failure to larger strains [11]. One such process is the continuous-bending-under-tension (CBT) process, which has demonstrated the ability to achieve plastic strains greater than those achieved by traditional forming processes that often trigger necking [12–14]. The process can also induce the process specific microstructural evolution.

The beneficial effect of superimposing bending on tension to enhance the elongation-to-fracture (ETF) of metal sheets was reported in Ref. [15] and then in sheet forming involving draw-beads [16]. During CBT testing and/or processing, the sheet is continuously bent-unbent by three rollers [12]. The rollers induce bending to the region of the sheet that is being incrementally deformed plastically. The sheet is deformed with a lower force, as the deformation is primarily achieved through the bending process underneath the rollers. More specifically, the deformation is concentrated in several small zones, i.e. two for each roll (bending/unbending), unless the pulling force is very high. As a result, localization of the deformation is delayed elongating the sheet incrementally beyond what can be achieved during standard simple tension (ST) [13]. Thus, the CBT process belongs to the incremental sheet forming (ISF) category of plastic deformation tests or processes [17]. Past research on AA6022-T4 has shown that the concentrated deformation in the fracture location upon ST is similar to the deformation over the entire gauge length of a CBT processed specimen [12,18]. For dual-phase steels, plastic deformation of the gauge section of a CBT specimen is even greater than in the fracture location of a ST specimen [19]. The CBT process basically delays the localization and necking, and as a result, facilitates a more uniform depletion of ductility

* Corresponding author. Department of Mechanical Engineering, University of New Hampshire, 33 Academic Way, Kingsbury Hall, W119, Durham, NH, 03824, USA.
E-mail address: marko.knezevic@unh.edu (M. Knezevic).

https://doi.org/10.1016/j.msea.2019.04.109
Received 12 March 2019; Received in revised form 23 April 2019; Accepted 29 April 2019
Available online 30 April 2019
0921-5093/

throughout the sheet as opposed to necking, where the reminder of the sheet has plenty of remaining ductility [17,19–21].

The interesting question is whether the origin of improved ETF and corresponding strength is material dependent or merely determined by the structural effects of the CBT test. Many similarities in the material behavior were observed after testing materials under CBT with similar mechanical properties [13,22,23]. If the CBT process is interrupted after a certain number of cycles, any residual ductility, as well as strength of the material, can be assessed by secondary tensile tests [22]. Taking the advantage that the strength is independent on the experimental CBT conditions from not at all to severe bending, stress-strain curves have been extrapolated to high strain levels based on measurements of the effective strain level and tensile strength by interrupting CBT tests after a certain number of cycles for a range of materials [22]. The level of hardening with CBT cycles successfully extrapolated the hardening achieved in a simple tensile test for some materials. Nevertheless, the authors have discussed the possibility of material effects influencing their results. The material effects have been observed in our recent CBT study for alloy AA6022-T4 [12], where the achieved level of hardening measured as a function of CBT cycles was observed to increase relative to the hardening in ST and then unusually decrease. However, some uncertainties in the testing procedure have been identified and discussed.

In this paper, strength and microstructure of alloy AA6022-T4 treated by CBT to a certain number of cycles is studied in more detail. We report strengthening, in material especially after treatment by first and the second CBT cycle processing. To understand the observed strengthening, we study microstructural evolution, including grain size, shape, texture, and dislocation substructures, using electron back scattered diffraction (EBSD) and transmission electron microscopy (TEM). We observe that the while the texture is evolving to form < 111 > fiber and grains elongate along the loading direction, precipitates do not change with CBT processing. We find that unlike in monotonic straining, cellular dislocation structures have developed within the grains after each pass of CBT. They are relatively loose after one CBT cycle but become more refined after subsequent cycles. To compare with monotonic ST, a finite element (FE) simulation of the process is performed to estimate the amount of strain in CBT. The results suggest that the combined tension plus forward and reverse bending of the CBT deformation led to the generation of substructure at much lower overall strain levels than under ST alone. In comparison, texture evolution, grain shape, and precipitates have only a secondary effect on the flow stress behavior after CBT. These findings reveal that the strength of the material after CBT testing is not only determined by the achieved effective strain level but actually dependent on the specific conditions during the CBT test inducing specific microstructural evolution. In particular, the propensity of the CBT to develop a well-defined substructure. As a result, estimating the post-necking material behavior based on measurements of the effective strain level and tensile strength by interrupting CBT tests after a certain number of cycles is not possible for the alloy. In closing, we show that the extrapolation of tensile material behavior to strain levels higher that achievable with ST alone is possible by matching measured load-displacement data during CBT by FE simulations of the process. These results are presented and discussed in this paper.

2. Material and experimental methods

This section describes the studied material, experimental procedures for testing and characterization along with details pertaining to an FE simulation of the CBT process.

2.1. Material

The material investigated in this study is a sheet of AA6022 heat treatable low copper, Al–Si–Mg alloy [24–28]. This widely used alloy offers an excellent combination of strength and formability. The material was in the temper T4 condition (AA6022-T4). Table 1 displays its chemical composition, which is obtained using Glow Discharge Spectrometry. The Mg and Si content are balanced to produce Mg_2Si precipitates [29]. It strengthens with the following precipitation sequence [30]: supersaturated solid solution $\alpha \rightarrow$ GP zones $\rightarrow$ needle-like β'' $\rightarrow$ rod-like β' + lath-like precipitates Q' $\rightarrow \beta$ + Si. The strengthening is due to the precipitate barriers to dislocation motion, with the β'' phase proving the most effective at increasing hardening [31]. The T4 heat treatment introduces nanoscale size precipitates into the grain boundaries and interiors [30–33].

Table 1
Chemical composition of alloy AA6022-T4 (wt%).

Si	Fe	Cu	Mn	Mg	Cr	Zn	Ti	Tin	Al
0.90	0.10	0.045	0.053	0.57	0.027	0.016	0.025	< 0.02	balance

2.2. Characterization methods

We used EBSD and TEM to characterize the microstructure before and after deformation. For EBSD, the samples were prepared using a Buehler EcoMet 3 grinding machine. A series of SiC grinding papers with different grit sizes, ranging from 180 to 1200, were used to grind the specimens. After grinding, 9 μm, 3 μm, and 1 μm polishing papers were used to polish the specimen. In the grinding and polishing steps water was used for the rinsing purposes. To achieve a better surface quality, polishing was continued using 0.05 μm, and 0.02 μm colloidal silica water based suspension. EBSD mapping was performed at a working distance of 10 mm and a step size of 1.5 μm. The accelerating voltage was set to be 30 kV. No cleaning is applied to the presented EBSD maps and points with a CI less than 0.1 are eliminated. The EBSD is presented only for the initial microstructure. The TEM analysis was performed on JEOL JEM-2100HR and FEI Tecnai G2 F30 microscopes [34–36]. The TEM samples were cut from CBT samples after 1x, 4x, and 6x cycles and from the failed tension samples. The observation directions are normal to the loading direction. The TEM samples were cut into 2 mm × 1 mm x 0.5 mm sheets along the rolling direction (RD), which was perpendicular to loading direction, and then gradually ground to approximately 40 μm, followed by dimpling and ion milling using a Gatan PIPS.

2.3. CBT processing

CBT deformation has been used in other works, typically using a universal testing machines equipped with a set of traversing rollers [13,14]. In the present study, the CBT deformation was applied using a custom experimental apparatus [12,18]. It is comprised of a moving carriage and a stationary roller assembly built on a base, as well as data-acquisition and control hardware and software. Unlike the other works, our apparatus has stationary rollers mounted on the machine base, while the specimen and its axial loading system is reciprocating. This enables use of digital image correlation (DIC) to study the strain accumulation per cycle, in real time. Also this set up is capable of processing both sheets and strips.

The carriage reciprocates during the CBT. It is built for a maximum (practical) speed of 66 m/s. After one forward motion, it receives signals to revert direction from limit switches, placed at the end of the stroke. Since the specimen may elongate after each stroke, one limit switch is placed on the moving crosshead of the hydraulic actuator. Another limit switch is attached to the roller assembly. There are three rollers all with the same diameter D = 25.4 mm. The axis to axis distance of the bottom two rollers is 54 mm. The top roller lies in between and its depth can be adjusted to achieve a desired bending depth, δ. The nominal strain imparted per roller engagement is 3.8% when the sheet

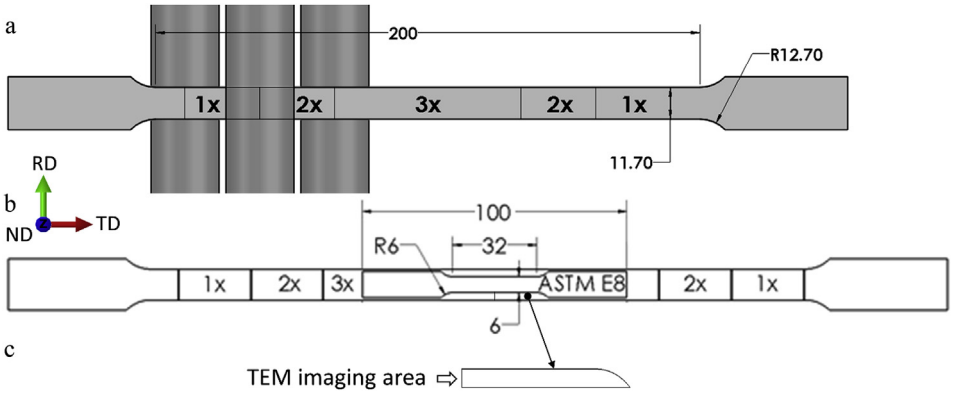

Fig. 1. (a) Initial CBT specimen. (b) Deformed CBT specimen along with the sub-size specimen for subsequent simple tension testing. The dimensions are in millimeters. The deformation regions (1x, 2x, and 3x) are indicated. (c) Removed volume of the CBT treated material used for the TEM imaging showing the observation direction.

of 1 mm wraps around it. The apparatus has two donut-style, Futek load-cells. The tension load cell (LCF 450, capacity of 22.24 kN) is attached to the hydraulic actuator and the compression load cell (LTH 500, capacity of 22.24 kN) is attached to the carriage. The position sensor on the actuator is a Balluff Micropulse BTL7-A501-M0305-Z-S32 with a resolution of 5 μm.

Fig. 1 shows a schematic of the CBT specimen with the different regions of deformation identified. The coordinates are marked as the rolling direction (RD), the transverse direction (TD) and the normal direction (ND). These regions correspond to the number of bending cycles the sheet undergoes during each CBT pass. Close to the grips region of the sheet only experiences one bending-unbending per cycle (1x), while the sheet in the central region of the sample is bent and unbent three times (3x). The gauge length of our CBT specimens is appropriately chosen to be 200 mm, considering the stroke of the machine [18,37–39]. The gauge section was lengthened from the standard ASTM E8 tensile specimen so that the rollers never exit the gauge section while producing the 1x, 2x, and 3x deformation regions. The CBT specimens were machined from a 1 mm thick AA6022-T4 sheet along TD. The CBT processing is carried out under a normalized bending depth of 2.5 and crosshead velocity of 1.2 mm/s. These processing parameters have been selected as they provided the greatest ETF facilitating the sheet undergoing 8 CBT cycles before fracture. Deformed CBT specimens are used to machine sub-size specimens for subsequent ST testing to evaluate the strength of the CBT treated sheets (Fig. 1b). The treated material is also used for microstructural characterization (Fig. 1c).

As described, CBT is a combination of bending and ST. In a research study, one could consider bending alone or ST alone as extremes to elucidate the effects of CBT on the material behavior. However, the wider the specimen and the larger the bend depth in CBT the closer the deformation mode imposed on the material is to plane strain tension, except the specimen edges, which are solely in tension [23]. In this work, we use a small-to-moderate bend depth and narrow strips. Thus, the deformation is much closer to tension than bending. Therefore, we compare the strengthening achieved in CBT to ST, which is a ubiquitous experiment to characterize the formability of sheet metal, rather than 3- or 4-point bending and CBT [40–42]. Moreover, from a practical point of attempting to infer post-necking strain hardening behavior of sheets by a combination of continuous bending under tension testing and finite element modeling, the reference is the ST test.

2.4. FE simulation set up

To estimate the stress and strain distribution with each CBT cycle, a finite element (FE) analysis using Abaqus was carried out. Fig. 2 shows the FE simulation set up and mesh, viewed at a tilt of 45°. Consistent with experiments, the simulations used a normalized bending depth of 2.5 and crosshead velocity of 1.2 mm/s. The velocity boundary conditions are directly applied to the sheet, while the rollers of D = 25.4 mm induce the bending, consistent with the experiment. The roller velocity profile recorded during the experiment is directly imported in the simulation. Half the FE model consisting of 9831 continuum 3D eight node elements with reduced integration (C3D8R) was simulated. The selected constitutive law was the rate-independent plasticity theory of von Mises (also known as J_2) with a yield surface that can expand isotropically, based on the given true stress-true strain curve for AA6022-T4 along TD. Since strain levels during CBT go beyond those measured during ST, the ST curve was appropriately extrapolated while matching the CBT load vs. displacement data (Fig. 3).

The measured and extrapolated true stress-true strain curves are shown in Fig. 4. The CBT enables much higher strains to be achieved than in ST. This result also implies that the CBT process can be used to extract post-necking material behavior. The post-necking strain hardening behavior is inferred by FE modeling of the measured load vs. displacement data under CBT. This result is significant because many sheet metal forming operations achieve high levels of plastic strain. To analyze or simulate these operations, the material behavior at these high levels of strain has to be known.

3. Results

The initial microstructure and crystallographic texture of the alloy was characterized using EBSD over a large area in two orthogonal planes: RD-ND and RD-TD. Fig. 5 shows the grain structure maps texture using the {001}, {011} and {111} pole figures for visualization. It can be seen that the starting material predominantly contains a cube texture component spread of moderate intensity. In the RD-TD frame grains exhibit an aspect ratio of 1:0.5. While there is some preference along RD, majority of the grains do not show a particular preference toward aligning with a particular direction. The scan in the RD-ND frame revealed an aspect ratio of 1:0.4 with a strong preference of grains aligned with the RD. As a result, an average major axis length of 50 μm provides an RD:TD:ND ellipsoidal grain with 50:34:20 μm dimensions, respectively.

Using TEM, precipitates of differing morphologies were found. Fig. 6 shows typical TEM images of globular, lath-like, rod-shaped, and larger boulder shaped precipitates. Lath-like precipitates lie in the boundaries and the remaining were dispersed within the grain interiors. These results are not surprising and are consistent with the globular, lath-like, and needle/rod-shaped, precipitates reported using TEM in other studies of this material [43]. GP zones have also been reported in this alloy [44], but these nanoscale precipitates are too fine to be seen via the TEM analysis here, and high-resolution TEM would be required. While these precipitates are a powerful strengthening mechanism, they, however, did not directly change with CBT cycles or explain differences between the CBT response and the ST response.

Fig. 7 shows engineering and true stress-strain curves measured in ST under a strain rate of 0.001/s along TD on samples of as-received initial sheet of AA6022-T4 and strips of the same material processed by

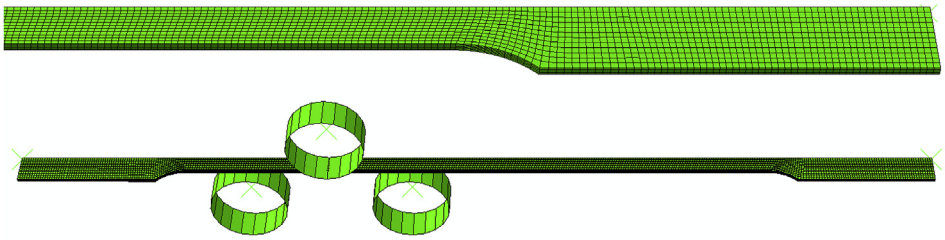

Fig. 2. Finite element simulation setup for the CBT process simulation in Abaqus under a normalized bending depth of 2.5 and crosshead velocity of 1.2 mm/s. The top image shows the initial mesh of the ½ FE model consisting of 9831C3D8R elements. The bottom image shows the rollers along before any engagement with the strip. The views are tilted at 45°.

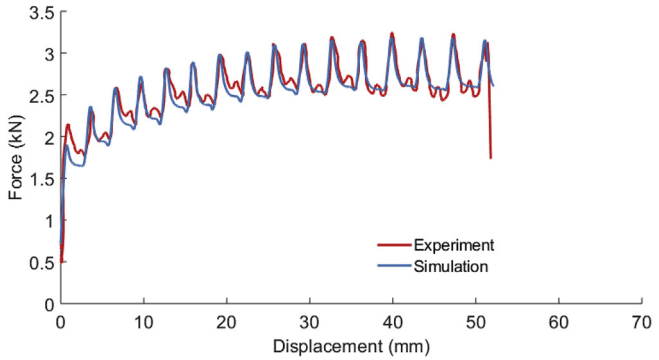

Fig. 3. Comparison between measured and simulated force vs. displacement curves during CBT under a crosshead velocity of 1.2 mm/s and a normalized bending depth of 2.5 along the TD.

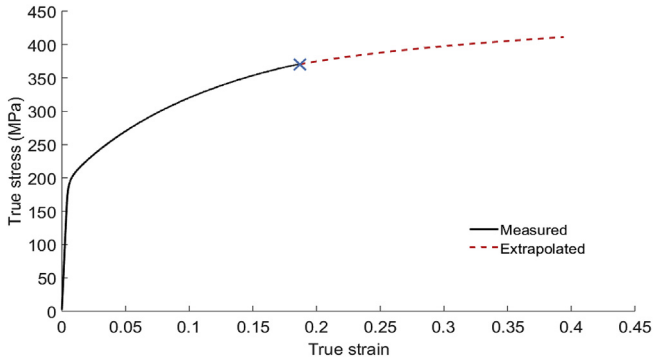

Fig. 4. True stress-strain curve for the initial material along the TD. The curve has been extrapolated to facilitate simulating the load vs. displacement data under CBT in Fig. 3.

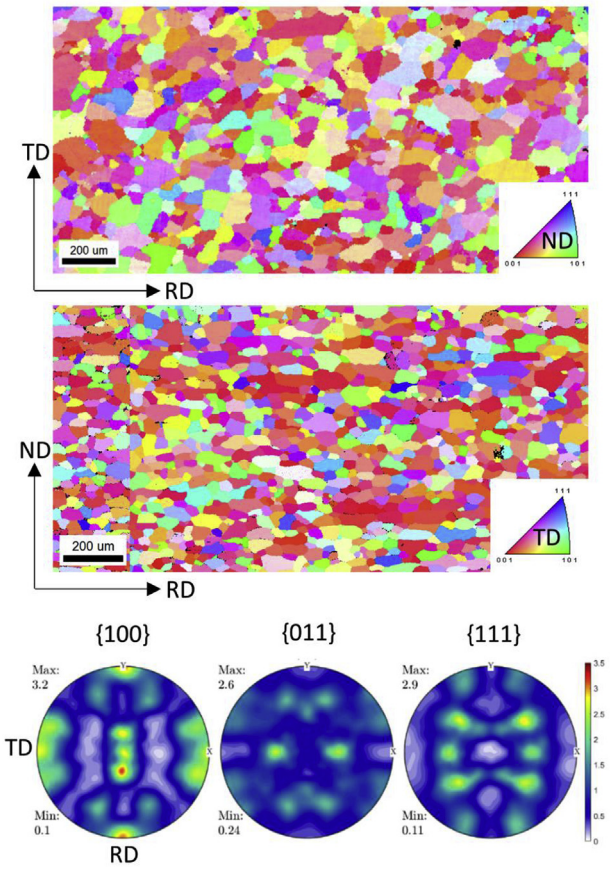

Fig. 5. Electron backscatter diffraction (EBSD) orientation maps showing grain structure and pole figures showing crystallographic texture of as received AA6022-T4.

CBT to 1, 2, 4, 6, and 8 number of CBT cycles. To assess the strengthening effect of CBT, the initial stress strain curve of the material is shown for comparison. The largest jump in strength occurs after the first two cycles. After the subsequent cycles, the strengthening is not as pronounced. As is evident, the elongation to failure reduces with the numbers of CBT cycles. Table 2 summarizes alloy properties based on the measurements.

Fig. 8 presents FE-calculated axial strain maps in the sample for five instances during CBT simulation. As before, the views are tilted at 45°. The model finds that some small amount of strain is introduced upon engagement of the rollers but before pulling (seen in Fig. 8b). The amount, however, is small compared to the strains generated after the second and fourth CBT cycles as shown in Fig. 8c and d, respectively. Distinct regions of strain have formed, with the most intense and largest region forming between 2x and 3x regions. This has been attributed to the geometrical discontinuity between the two regions [19]. The strain regions become less intense in regions 2x and 1x closer to the ends. As seen in Fig. 8e and f, strain distributions after six CBT cycles and at failure, which happened before completing the eighth CBT cycle, are similar to those established at the second cycle but clearly the accumulated strains have increased. Axial strain, LE11, is predicted to accumulate with CBT cycles from 0.0431 in the first CBT cycle to over 0.0814, 0.1192, 0.157, 0.195, 0.2336, 0.272, and 0.293 in subsequent cycles 1x to 8x, respectively. These values were taken from the central region (in the middle of the 3x region) of the sample, where the strains are relatively uniform.

In Fig. 8f, it is especially noticeable that axial strain concentrates at the boundary between 2x and 3x deformation regions, which is where failures in the experiments are observed as well. We will refer to this region as a hot spot. The corresponding strain levels in the hot spots, where the strain concentrations are exceptionally high, are 0.05239, 0.09068, 0.13309, 0.17688, 0.21947, 0.26076, 0.30494, and 0.34871. The flow stress curve in Fig. 4 was extrapolated sufficiently to cover these strain levels.

Returning to the observed strength data, we find that after two CBT cycles, the yield strength increases from 185 MPa to 297 MPa and the ultimate tensile strength (UTS) from 307 MPa to 345 MPa. In comparison, the flow stress in ST after the same amount of strain as after two CBT cycles is only 270 MPa. Therefore, compared to ST loading to the

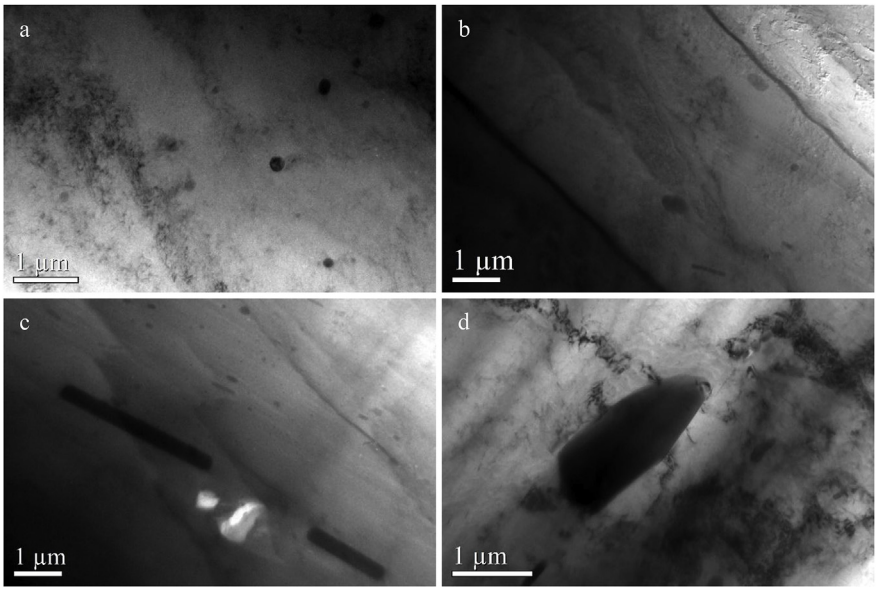

Fig. 6. TEM images showing precipitate types in the alloy AA6022: (a) globular, (b) lath-like, (c) rod-like, and (d) unusually large. The scale bar in each image is 1 μm.

same accumulated strain, the strengthening obtained via CBT is remarkably large. It is also worth noting that the total accumulated strain in CBT is relatively low. Thus, the CBT pathway engenders much more strengthening than would be expected for the total amount of accumulated strain.

The question then remains as to why does CBT result in such large amounts of strengthening with little accumulated strain? The likely explanation is that the microstructure generated under CBT must be different than that which evolves in ST. We carried out EBSD and TEM in order to evaluate the texture and dislocation structures in the interior of the grains. As already reported in Ref. [12], the texture evolves during CBT to a < 111 > fiber texture along the tension axis. The same texture evolution occurs in ST loading as well [12,45–48]. However, under CBT, texture development evolves more because the accumulated strain is higher than in ST, which is to be expected. To sum, in both CBT and ST, the grains elongate in the RD direction (tensile axis) and a < 111 > fiber texture develops along the tensile axis. The degree to which these microstructural features change scales with accumulated strain and therefore are more pronounced in CBT with increased cycles than in the tensile regions in the same strip.

Next, the dislocation structure development inside the grains were analyzed as another possible contribution to the strengthening. Figs. 9–12 show TEM images of typical dislocation structures in grains after ST (to failure strains), after 1x, 4x, and 6x CBT cycles. The striking difference is that in ST, dislocations are uniformly distributed in the grains, whereas after CBT, dislocation cell structures develop after 1x, 4x, and 6x CBT cycles. These cell structures are seen to refine with CBT pass, from dislocation from loose tangles of dislocations in the 1x CBT sample to dislocation cells in the 4x and 6x CBT samples.

4. Discussion

This is the first time intragranular cell structures have been analyzed in material deformed by CBT. In comparison, numerous studies have reported similar cell dislocation structure development in single crystalline and polycrystalline face-centered cubic (fcc) materials, like copper, nickel, and aluminum, which have been deformed under large strain rolling, ST, simple compression, forward-reverse loading, and cyclic loading [49–58]. In these works, cell structures were similarly characterized by relatively dislocation-depleted regions called cells enclosed by dense cell walls or tangles. The presence of these cell walls can hinder slip and result in strain hardening, which would explain the strengthening seen in the CBT material that was achieved as subgrain structures developed between the 1x and 4x CBT cycles. In AA6022-T4, conventional deformation processing is found to cause uniform dislocation distributions, displaying occasional faint cell wall formation, to develop within the grains [59]. Consistent with this earlier observation, we confirm that dislocation structures formed during ST of this alloy up

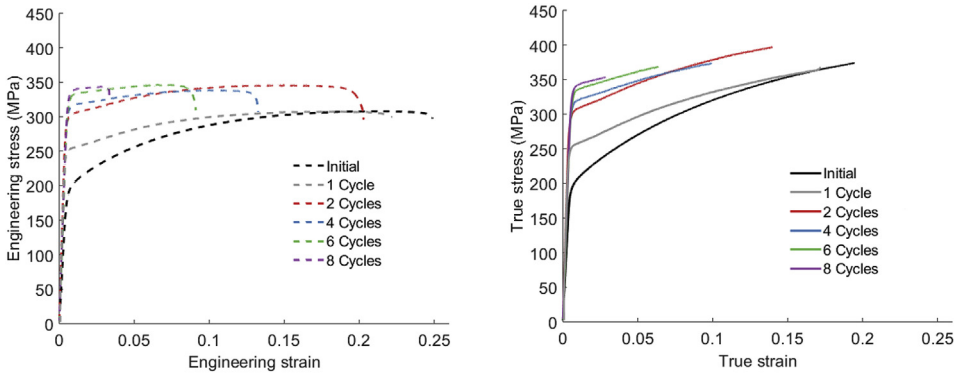

Fig. 7. Engineering stress-strain and true stress-strain curves measured in simple tension under a strain rate of 0.001/s along the transverse direction (TD) on samples of as-received initial sheet of AA6022-T4 and strips of the same material processed by CBT to the number of cycles as indicated in the legends.

Table 2
Properties based on the flow curves from Fig. 7.

	ST	# of CBT cycle				
		1	2	4	6	8
Yield stress (MPa)	185	249	297	310	327	332
UTS (MPa)	307	307	345	338	346	343
Strain at UTS	0.217	0.188	0.15	0.104	0.066	0.029
Strain at fracture	0.249	0.222	0.203	0.133	0.091	0.034

to 25% strain are disorganized and not as well defined. However, CBT permits larger strain levels than the ST test and the deformation states are not as simple. Substructure development has been found to depend on strain level as well as grain orientation, which could explain the difference in substructure morphology seen here in CBT vs ST. In an extensive and detailed study of subgrain structure evolution in aluminum with similar grain sizes 300 μm and von Mises strains to 0.34 as in the CBT material, Huang and Hansen [50] found a strong correlation between cellular substructure development and grain orientation. Cell substructure tended to develop in grains with their tensile axis lying near the [100] corner, a state of stress that promotes multiple slip. We note that CBT also differs from ST due to the repeated forward-reverse bending cycles. In pure Al, even after a few percent to 10% strain in ST [49], similar cellular structures as seen here were reported to form within grains. In cyclic loading, during the reverse loading, Hasagawa found the cellular structure to dissolve, only to be reformed at the end of reverse loading stroke. Hence subgrain cellular structures, although not stable, persist in cyclic loading. In CBT, the deformation is very different from pure cyclic loading since the bending cycles are incrementally superimposed with tension. It has been reported in Cu that cyclic loading with a positive mean stress tends to promote cellular substructure development over localized slip banding [60]. The explanation put forth is that the complex stress states promote multiple slip, which again leads to development of cellular structures over localized bands. This reasoning is sufficiently general to apply to the fcc Al alloy studied here. In contrast, the work on DP 1180 steel [19], did not find as high level of strengthening during CBT as for the alloy AA6022-T4. The steel had much finer grain size, two phases of contrasting strength, and different texture, which likely reduced the propensity of the microstructure to form dislocation substructures. The observation for DP 1180 suggests that the explanation for strengthening of the alloy AA6022-T4 by the cell structures refinement is indeed sensible.

Based on this analysis we can speculate on the relationship between substructure development and the stress-strain response of CBT-treated sheet. Recall that the largest jump in strength occurs after the first two cycles, which coincides with the dramatic change when going from the initial material with no substructure to the material containing dislocation substructures. After the subsequent cycles, the strengthening persists but is not as significant, again consistent with the minimal changes in dislocation substructure patterns after 4x CBT cycles. Eventually with more CBT passes, dislocations would be expected to pile up at the dislocation substructures, thereby leading to a void formation. Al alloys are known to fracture due to localizations induced by crystallographic slip [61]. Micrographs taken by a scanning electron microscope of the sample deformed in CBT showed evidence of ductile damage formation in terms of particle fragmentation and decohesion from the matrix throughout the specimen without necking [12]. In contrast, samples broken in ST showed that damage in terms of particle fragmenting develops locally and quickly leads to necking and fracture. No damage was found away from the necked region in ST.

The dislocation substructure development seen here may also elucidate a possible reason for the enhanced ETF under CBT. Enhanced ductility or formability in steels can arise when the metal experiences intermittent relaxation [62–64]. While the deformation is held or

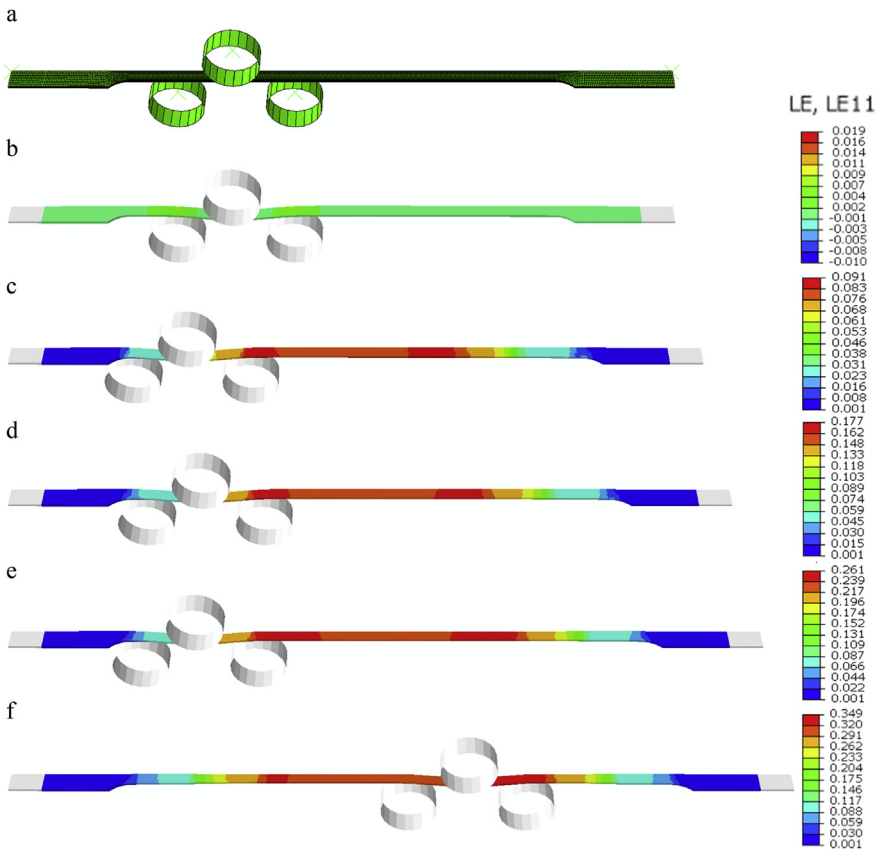

Fig. 8. Axial strain contours developing during the CBT process simulated in Abaqus: (a) before any engagement of the rollers, (b) upon engagement of the rollers but before pulling, (c) after 2 CBT cycles, (d) after 4 CBT cycles, (e) after 6 CBT cycles, and (f) at failure, which happened before completing the 8th CBT cycles. The views are tilted at 45°.

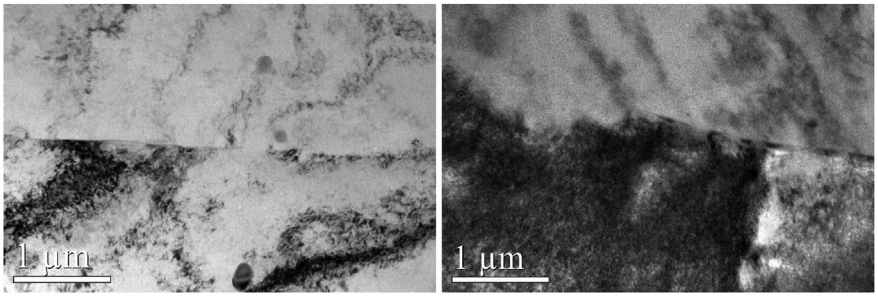

Fig. 9. Dislocation structures developed within grains after simple tension in the necked region. Images are from the necked region meaning that the strain level is higher than in the gage region. Loose dislocation tangles, and no dislocation patterns, such as cell structures, are observed. The scale bar in images is 1 μm.

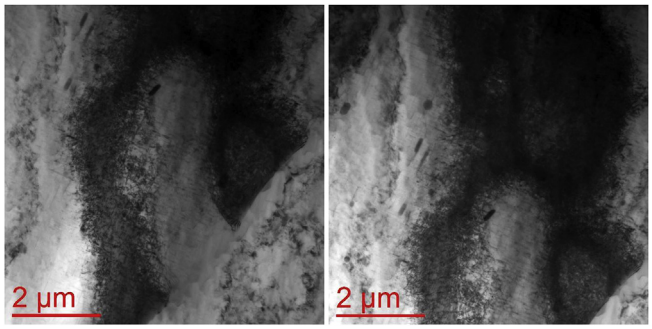

Fig. 10. Dislocation structures after 1 cycle of CBT. As is evident, loose tangles of dislocations have developed. According to the FE analysis, the strain in the central region of region 3x is 0.0431. The scale bar in images is 2 μm.

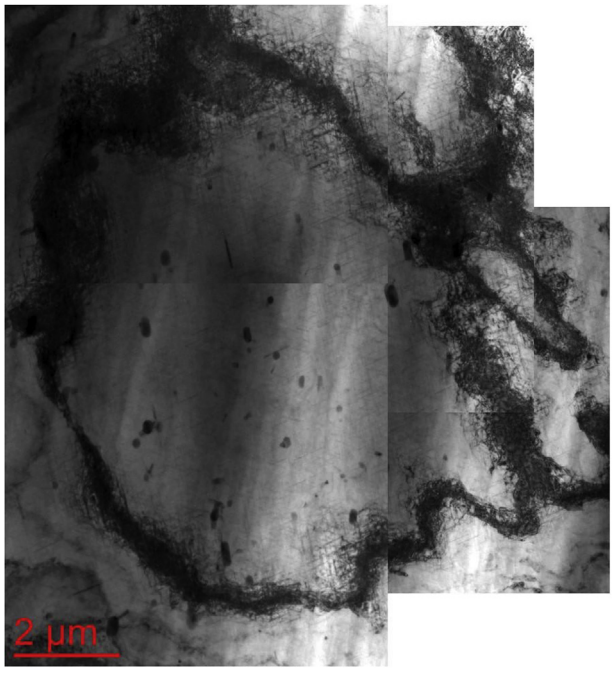

Fig. 11. Dislocation cell structures after 4 cycles of CBT. According to the FE analysis, the strain in the central region of region 3x is 0.157. The scale bar is 2 μm.

stopped intermittently, it is conjectured that dislocation density reduces or reconfigures to low energy substructures [64]. The rearrangement permits the internal stresses to relax or homogenize removing any unwanted stress concentrations [63]. As shown in Fig. 4, the stress-strain curve in CBT extends to higher strain levels than the same material in ST. In CBT, relaxation due to the loading-unloading in bending could have facilitated the development of the underlying stored dislocations

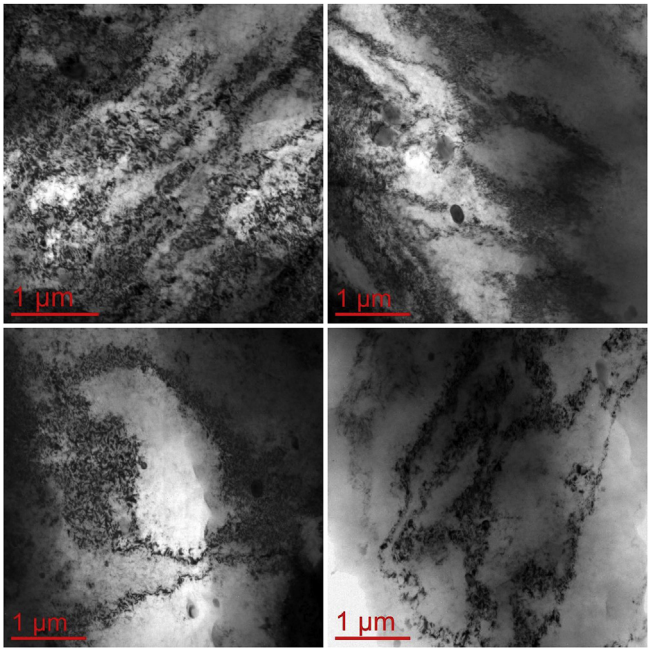

Fig. 12. Dislocation cell structures after 6 cycles of CBT. According to the FE analysis, the strain in the central region of region 3x is 0.2336. The scale bar in images is 1 μm.

to reconfigure into low energy cell structures. The work presented here has also shown that the CBT test can be considered as a test method for determining the hardening behavior of sheet metals at high levels of elongation.

5. Conclusions

In this paper, we report improvements in strength after continuous-bending-under-tension (CBT) treatments of alloy AA6022-T4 sheets. After only one or two CBT cycles, the strength enhancements are significant but with further cycling, the improvements were incremental. These observations are rationalized by calculating using finite element simulation the amount of strain accumulated during CBT and characterizing microstructural evolution using electron microscopy. Significantly, the combination of the FE simulation and CBT data facilitated inferring of the post-necking behavior of the alloy. The detailed microstructural analysis indicates that differences in texture evolution, grain shape and grain size evolution were not appreciable between CBT and ST or with CBT cycling. Also, the precipitates did not change during CBT cycle. Yet strengthening with CBT cycling was found to continue, even up to eight CBT cycles. Evidently these microstructural features have only a secondary effect on the strengthening in the material after the CBT treatment. In contrast, we show significant differences in the dislocation patterns between ST and CBT cases. No

dislocation cell structures were observed in the ST sample deformed to failure yet dislocation cells developed in 1x, 4x and 6x samples. The dislocation configurations transitioned from dislocation tangles in the 1x CBT sample to dislocation cells in the 4x and 6x samples. These findings reveal that the strength of the material after CBT testing is determined by the achieved effective strain level and the propensity of the CBT to develop a well-defined substructure.

Data availability

The raw/processed data required to reproduce these findings cannot be shared at this time due to technical or time limitations.

Acknowledgments

The authors gratefully acknowledge support from the U.S. National Science Foundation (NSF) under grant No. CMMI-1727495 (UNH) and CMMI-1728224 (UCSB).

Appendix A. Supplementary data

Supplementary data to this article can be found online at https://doi.org/10.1016/j.msea.2019.04.109.

References

[1] B. Ma, Z.G. Liu, Z. Jiang, X. Wu, K. Diao, M. Wan, Prediction of forming limit in DP590 steel sheet forming: an extended fracture criterion, Mater. Des. 96 (2016) 401–408.
[2] W.S. Miller, L. Zhuang, J. Bottema, A.J. Wittebrood, P. De Smet, A. Haszler, A. Vieregge, Recent development in aluminium alloys for the automotive industry, Mater. Sci. Eng. 280 (2000) 37–49.
[3] J. Hirsch, T. Al-Samman, Superior light metals by texture engineering: optimized aluminum and magnesium alloys for automotive applications, Acta Mater. 61 (2013) 818–843.
[4] M. Bhargava, S. Chakrabarty, V.K. Barnwal, A. Tewari, S.K. Mishra, Effect of microstructure evolution during plastic deformation on the formability of transformation induced plasticity and quenched & partitioned AHSS, Mater. Des. 152 (2018) 65–77.
[5] A.M. Cantara, M. Zecevic, A. Eghtesad, C.M. Poulin, M. Knezevic, Predicting elastic anisotropy of dual-phase steels based on crystal mechanics and microstructure, Int. J. Mech. Sci. 151 (2019) 639–649.
[6] M. Zecevic, Y.P. Korkolis, T. Kuwabara, M. Knezevic, Dual-phase steel sheets under cyclic tension–compression to large strains: experiments and crystal plasticity modeling, J. Mech. Phys. Solids 96 (2016) 65–87.
[7] C.C. Tasan, J.P.M. Hoefnagels, M. Diehl, D. Yan, F. Roters, D. Raabe, Strain localization and damage in dual phase steels investigated by coupled in-situ deformation experiments and crystal plasticity simulations, Int. J. Plast. 63 (2014) 198–210.
[8] P. Henn, M. Liewald, M. Sindel, Characterising ductility of 6xxx-series aluminium sheet alloys at combined loading conditions, AIP Conf. Proc. 1896 (2017) 020008.
[9] J. Hirsch, Recent development in aluminium for automotive applications, Trans. Nonferrous Metals Soc. China 24 (2014) 1995–2002.
[10] H. Zarei, Experimental and Numerical Investigation of Crash Structures Using Aluminum Alloys, Cuvillier Verlag, Göttingen, Germany, 2008.
[11] O. Music, J. Allwood, K. Kawai, A review of the mechanics of metal spinning, J. Mater. Process. Technol. 210 (2010) 3–23.
[12] M. Zecevic, T. Roemer, M. Knezevic, Y. Korkolis, B. Kinsey, Residual ductility and microstructural evolution in continuous-bending-under-tension of AA-6022-T4, Materials 9 (2016) 130.
[13] W.C. Emmens, A.H. van den Boogaard, Incremental forming by continuous bending under tension—an experimental investigation, J. Mater. Process. Technol. 209 (2009) 5456–5463.
[14] J. Benedyk, N. Parikh, D. Stawarz, A method for increasing elongation values for ferrous and nonferrous sheet metals, J. Mater. 6 (1971) 16–29.
[15] H. Swift, Plastic bending under tension, Engineering 166 (1948) 333–359.
[16] H. Nine, Drawbead Forces in Sheet Metal Forming. Mechanics of Sheet Metal Forming, Springer, Boston, MA, 1978, pp. 179–211.
[17] W.C. Emmens, A.H. van den Boogaard, An overview of stabilizing deformation mechanisms in incremental sheet forming, J. Mater. Process. Technol. 209 (2009) 3688–3695.
[18] T.J. Roemer, T.J. Barrett, M. Knezevic, B.L. Kinsey, Y.P. Korkolis, Experimental study of continuous-bending-under-tension of AA6022-T4, J. Mater. Process. Technol. 266 (2019) 707–714.
[19] C.M. Poulin, Y.P. Korkolis, B.L. Kinsey, M. Knezevic, Over five-times improved elongation-to-fracture of dual-phase 1180 steel by continuous-bending-under-tension, Mater. Des. 161 (2019) 95–105.
[20] W.C. Emmens, G. Sebastiani, A.H. van den Boogaard, The technology of Incremental Sheet Forming—a brief review of the history, J. Mater. Process. Technol. 210 (2010) 981–997.
[21] J.M. Allwood, D.R. Shouler, A.E. Tekkaya, The increased forming limits of incremental sheet forming processes, Key Eng. Mater. 344 (2007) 621–628.
[22] W. Emmens, A.H. van den Boogaard, Material characterization at high strain by adapted tensile tests, Exp. Mech. 52 (2012) 1195–1209.
[23] W.C. Emmens, A.H. van den Boogaard, Cyclic stretch-bending: mechanics, stability and formability, J. Mater. Process. Technol. 211 (2011) 1965–1981.
[24] Alcoa. Alloy 6022 Sheet, North American Rolled Products.
[25] M. Zecevic, M. Knezevic, Latent hardening within the elasto-plastic self-consistent polycrystal homogenization to enable the prediction of anisotropy of AA6022-T4 sheets, Int. J. Plast. 105 (2018) 141–163.
[26] M. Zecevic, M. Knezevic, Modeling of sheet metal forming based on implicit embedding of the elasto-plastic self-consistent formulation in shell elements: application to cup drawing of AA6022-T4, J. Occup. Med. 69 (2017) 922–929.
[27] M. Zecevic, M. Knezevic, A dislocation density based elasto-plastic self-consistent model for the prediction of cyclic deformation: application to Al6022-T4, Int. J. Plast. 72 (2015) 200–217.
[28] M. Zecevic, I.J. Beyerlein, M. Knezevic, Coupling elasto-plastic self-consistent crystal plasticity and implicit finite elements: applications to compression, cyclic tension-compression, and bending to large strains, Int. J. Plast. 93 (2017) 187–211.
[29] A. Jaafar, A. Rahmat, l. Zainol, Z. Hussain, Effects of composition on the mechanical properties and microstructural development of dilute 6000 series alloys, J. Appl. Sci. 12 (2012) 775–780.
[30] W.F. Miao, D.E. Laughlin, Precipitation hardening in aluminum alloy 6022, Scripta Mater. 40 (1999) 873–878.
[31] D.G. Eskin, M.L. Kharakterova, The effect of silicon and copper on the precipitation hardnening of sheets of 6xxx series alloy, Mater. Technol. 35 (2001) 5–8.
[32] P. Trivedi, D.P. Field, H. Weiland, Alloying effects on dislocation substructure evolution of aluminum alloys, Int. J. Plast. 20 (2004) 459–476.
[33] R.S. Yassar, D.P. Field, H. Weiland, Transmission electron microscopy and differential scanning calorimetry studies on the precipitation sequence in an Al–Mg–Si alloy: AA6022, J. Mater. Res. 20 (2005) 2705–2711.
[34] M. Jahedi, I.J. Beyerlein, M.H. Paydar, S. Zheng, T. Xiong, M. Knezevic, Effects of pressure and number of turns on microstructural homogeneity developed in high-pressure double torsion, Metall. Mater. Trans. 48 (2017) 1249–1263.
[35] M. Jahedi, M.H. Paydar, S. Zheng, I.J. Beyerlein, M. Knezevic, Texture evolution and enhanced grain refinement under high-pressure-double-torsion, Mater. Sci. Eng. 611 (2014) 29–36.
[36] M. Knezevic, J.S. Carpenter, M.L. Lovato, R.J. McCabe, Deformation behavior of the cobalt-based superalloy Haynes 25: experimental characterization and crystal plasticity modeling, Acta Mater. 63 (2014) 162–168.
[37] D.H. Smith, J. Bicknell, L. Jorgensen, B.M. Patterson, N.L. Cordes, I. Tsukrov, M. Knezevic, Microstructure and mechanical behavior of direct metal laser sintered Inconel alloy 718, Mater. Char. 113 (2016) 1–9.
[38] S. Ghorbanpour, B.A. McWilliams, M. Knezevic, Effect of hot working and aging heat treatments on monotonic, cyclic, and fatigue behavior of WE43 magnesium alloy, Mater. Sci. Eng. 747 (2019) 27–41.
[39] S. Gribbin, J. Bicknell, L. Jorgensen, I. Tsukrov, M. Knezevic, Low cycle fatigue behavior of direct metal laser sintered Inconel alloy 718, Int. J. Fatigue 93 (1) (2016) 156–167.
[40] S. Gribbin, S. Ghorbanpour, N.C. Ferreri, J. Bicknell, I. Tsukrov, M. Knezevic, Role of grain structure, grain boundaries, crystallographic texture, precipitates, and porosity on fatigue behavior of Inconel 718 at room and elevated temperatures, Mater. Char. 149 (2019) 184–197.
[41] M. Knezevic, R.J. McCabe, R.A. Lebensohn, C.N. Tomé, C. Liu, M.L. Lovato, B. Mihaila, Integration of self-consistent polycrystal plasticity with dislocation density based hardening laws within an implicit finite element framework: application to low-symmetry metals, J. Mech. Phys. Solids 61 (2013) 2034–2046.
[42] M. Knezevic, R.A. Lebensohn, O. Cazacu, B. Revil-Baudard, G. Proust, S.C. Vogel, M.E. Nixon, Modeling bending of α-titanium with embedded polycrystal plasticity in implicit finite elements, Mater. Sci. Eng. 564 (2013) 116–126.
[43] K. Teichmann, C.D. Marioara, S.J. Andersen, K. Marthinsen, TEM study of β′ precipitate interaction mechanisms with dislocations and β′ interfaces with the aluminium matrix in Al–Mg–Si alloys, Mater. Char. 75 (2013) 1–7.
[44] R.S. Yassar, D.P. Field, H. Weiland, The effect of predeformation on the β″ and β′ precipitates and the role of Q′ phase in an Al–Mg–Si alloy; AA6022, Scripta Mater. 53 (2005) 299–303.
[45] M. Knezevic, S.R. Kalidindi, D. Fullwood, Computationally efficient database and spectral interpolation for fully plastic Taylor-type crystal plasticity calculations of face-centered cubic polycrystals, Int. J. Plast. 24 (2008) 1264–1276.
[46] M. Knezevic, S.R. Kalidindi, R.K. Mishra, Delineation of first-order closures for plastic properties requiring explicit consideration of strain hardening and crystallographic texture evolution, Int. J. Plast. 24 (2008) 327–342.
[47] M. Knezevic, N.W. Landry, Procedures for reducing large datasets of crystal orientations using generalized spherical harmonics, Mech. Mater. 88 (2015) 73–86.
[48] M. Knezevic, M. Zecevic, I.J. Beyerlein, R.A. Lebensohn, A numerical procedure enabling accurate descriptions of strain rate-sensitive flow of polycrystals within crystal visco-plasticity theory, Comput. Methods Appl. Mech. Eng. 308 (2016) 468–482.
[49] T. Hasegawa, T. Yakou, S. Karashima, Deformation behaviour and dislocation structures upon stress reversal in polycrystalline aluminium, Mater. Sci. Eng. 20 (1975) 267–276.
[50] X. Huang, N. Hansen, Grain orientation dependence of microstructure in aluminium deformed in tension, Scripta Mater. 37 (1997) 1–7.
[51] K.A. Lurie, A stable spatio-temporal G-closure and Gm-closure of a set of isotropic dielectrics with respect to one-dimensional wave propagation, Wave Motion 40

(2004) 95–110.
[52] H. Christoffersen, T. Leffers, Microstructure and composite deformation pattern for rolled brass, Scripta Mater. 37 (1997) 1429–1434.
[53] X. Huang, Grain orientation effect on microstructure in tensile strained copper, Scripta Mater. 38 (1998) 1697–1703.
[54] G. Winther, D.J. Jensen, N. Hansen, Dense dislocation walls and microbands aligned with slip planes—theoretical considerations, Acta Mater. 45 (1997) 5059–5068.
[55] D.A. Hughes, N. Hansen, Microstructure and strength of nickel at large strains, Acta Mater. 48 (2000) 2985–3004.
[56] D.A. Hughes, N. Hansen, Microstructural evolution in nickel during rolling from intermediate to large strains, MTA 24 (1993) 2022–2037.
[57] D.A. Hughes, W.D. Nix, The absence of steady-state flow during large strain plastic deformation of some Fcc metals at low and intermediate temperatures, MTA 19 (1988) 3013–3024.
[58] B. Bay, N. Hansen, D. Kuhlmann-Wilsdorf, Deformation structures in lightly rolled pure aluminium, Mater. Sci. Eng. 113 (1989) 385–397.
[59] J.W. Yoon, F. Barlat, J.J. Gracio, E. Rauch, Anisotropic strain hardening behavior in simple shear for cube textured aluminum alloy sheets, Int. J. Plast. 21 (2005) 2426–2447.
[60] P. Lukáš, L. Kunz, Cyclic plasticity and substructure of metals, Mater. Sci. Eng. 322 (2002) 217–227.
[61] A.J. Gross, K. Ravi-Chandar, On the deformation and failure of Al 6061-T6 in plane strain tension evaluated through in situ microscopy, Int. J. Fract. 208 (2017) 27–52.
[62] K. Hariharan, O. Majidi, C. Kim, M. Lee, F. Barlat, Stress relaxation and its effect on tensile deformation of steels, Mater. Des. 52 (2013) 284–288 (1980-2015).
[63] K. Hariharan, P. Dubey, J. Jain, Time dependent ductility improvement of stainless steel SS 316 using stress relaxation, Mater. Sci. Eng. 673 (2016) 250–256.
[64] A. Varma, A. Gokhale, J. Jain, K. Hariharan, P. Cizek, M. Barnett, Investigation of stress relaxation mechanisms for ductility improvement in SS316L, Phil. Mag. 98 (2018) 165–181.